



1 **Tectonic interactions during rift linkage: Insights from analog and numerical**
2 **experiments**

3

4 *Timothy Chris Schmid¹, Sascha Brune^{2,3}, Anne Glerum², and Guido Schreurs¹*

5

6 ¹*Institute of Geological Sciences, University of Bern*

7 ²*Helmholtz Centre Potsdam – GFZ German Research Centre for Geosciences, Potsdam, Germany*

8 ³*University of Potsdam, Potsdam-Golm, Germany*

9

10 *Corresponding author Timothy Schmid: timothy.schmid@geo.unibe.ch*

11 *Institute of Geological Sciences, University of Bern, Baltzerstrasse 1+3, CH-3012 Bern, Switzerland*

12

13 **Keywords:** *Numerical modelling, analog modelling, stress deflection, rift interaction, rift*
14 *propagation*

15

16 **Abstract**

17 Continental rifts evolve by linkage and interaction of adjacent individual segments. As rift
18 segments propagate, they can cause notable re-orientation of the local stress field so that
19 stress orientations deviate from the regional trend. In return, this stress re-orientation can feed
20 back on progressive deformation and may ultimately deflect propagating rift segments in an
21 unexpected way. Here, we employ numerical and analog experiments of continental rifting to
22 investigate the interaction between stress re-orientation and segment linkage. Both model
23 types employ crustal-scale two-layer setups where pre-existing linear heterogeneities are
24 introduced by mechanical weak seeds. We test various seed configurations to investigate the
25 effect of i) two competing rift segments that propagate unilaterally, ii) linkage of two opposingly
26 propagating rift segments, and iii) the combination of these configurations on stress re-
27 orientation and rift linkage. Both the analog and numerical models show counter-intuitive rift
28 deflection of two rift segments competing for linkage with an opposingly propagating segment.
29 The deflection pattern can be explained by means of stress analysis in numerical experiments
30 where stress re-orientation occurs locally and propagates across the model domain as rift
31 segments propagate. Major stress re-orientations may occur locally, which means that faults
32 and rift segment trends do not necessarily align perpendicularly to far-field extension
33 directions. Our results show that strain localization and stress re-orientation are closely linked,



34 mutually influence each other and may be an important factor for rift deflection among
35 competing rift segments as observed in nature.

36

37 **1. Introduction**

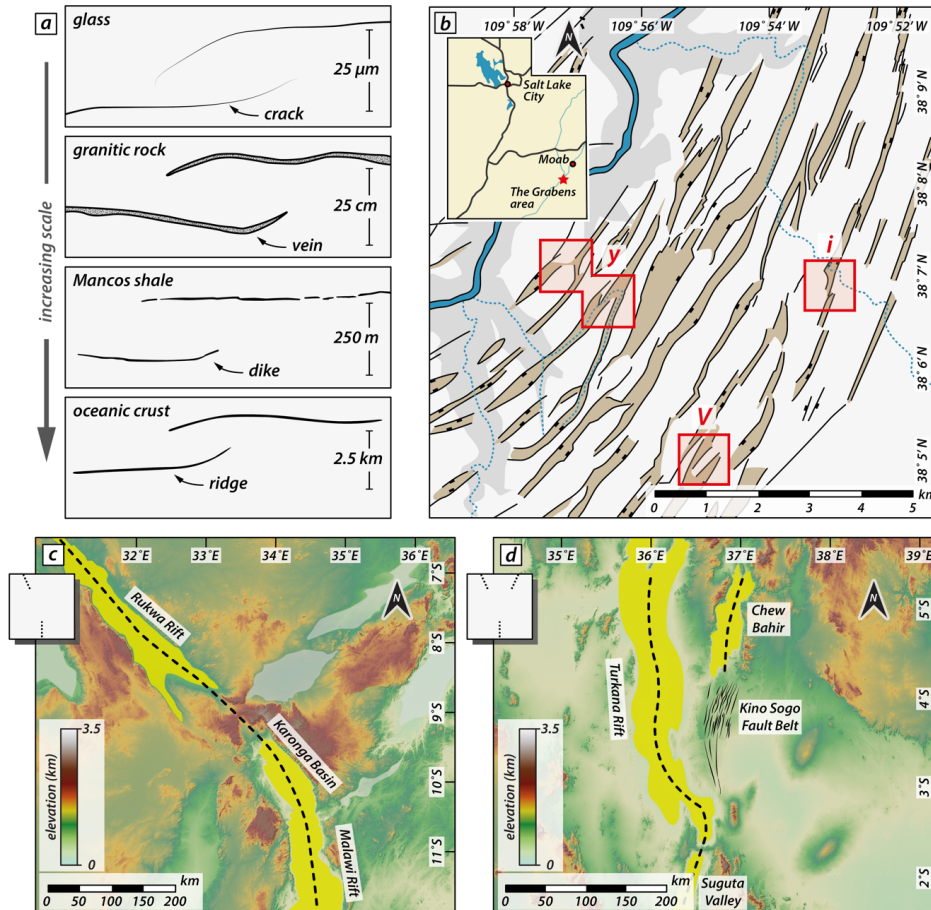
38 Continental rifting involves brittle faulting and the formation of subsiding rift basins. In places
39 where individual rift segments are in proximity, they may interact and link when segments
40 propagate and the rift system matures (Morley et al., 1990; Nelson et al., 1992; Rosendahl, 1987).

41 The propagation and linkage of formerly isolated rift segments resembles the propagation and
42 interaction of extension fractures on a micro-scale (e.g., Childs et al., 1995; Willemse, 1997;
43 Willemse et al., 1996; Fig. 1a). Indeed, analytical solutions and models have been used to
44 describe crack growth and to predict its direction (e.g., Macdonald and Fox, 1983; Mills, 1981).
45 Such cracks occur in a variety of materials over a vast order of magnitude in length scale from
46 micro-scale cracks in glass to km-scale ridge interaction structures in oceanic crust (Pollard and
47 Aydin, 1984; Fig. 1a).

48

49 Propagation and interaction of individual rift segments occur in continental rift systems at
50 various scales and have been intensively studied over the years. The East African Rift System
51 (EARS) constitutes a narrow rift with an eastern and western branch that propagate southward
52 and northward, respectively (EARS; e.g., Bonini et al., 2005; Bosworth, 1985; Brune et al., 2017;
53 Corti et al., 2019; Ebinger et al., 2000; Glerum et al., 2020; Heilman et al., 2019; Koehn et al.,
54 2008; Kolawole et al., 2018; Morley et al., 1990; Nelson et al., 1992). On smaller scale, interaction
55 of segmented grabens has been studied for example in in the Canyonlands National Park, Utah,
56 a part of the Basin and Range wide rift (Allken et al., 2013; Schultz-Ela and Walsh, 2002; Trudgill,
57 2002), where various styles of graben interaction are attributed to the underlying strata (e.g.,
58 salt layer) or pre-existing weaknesses (Fig. 1b).

59



60
61

62 **Figure 1:** Similar linkage structures occurring at a vast range of spatial scales. a) Propagation and linkage of segments at
63 different scale from micro cracks in glass to linkage of oceanic ridge segments. Redrawn after Pollard and Aydin (1984). b)
64 Rift-related linked graben structures in the Canyonlands National Park, USA. Red rectangles mark areas with distinct
65 interaction geometries (v-, i-, and y-geometries; see text for detail). Redrawn after Allken et al. (2013). c) Rukwa Rift and
66 North Malawi rift in the western branch of the East African Rift System (EARS). The two basins link obliquely via the Karonga
67 Basin and form an interaction zone. Rift axes redrawn after Kolawole et al. (2021). d) Turkana Rift on the eastern branch of
68 the EARS. The southward propagating Turkana Rift links with the Suguta Valley that propagates northwards. To the east, the
69 Kino Sogo Fault Belt (KSF) forms the continuation of the Chew Bahir basin which is part of the Kenyan Rift. Rift axes and
70 faults redrawn after Corti et al. (2019) and Vétel et al. (2005), respectively. Grey insets refer to the geometry of the initial pre-
71 existing weaknesses prior to basin evolution (see text for details).

72

73 Structural inheritance is thought to control nucleation and strain distribution along newly
74 formed normal faults as weak fabrics can precondition and weaken a heterogeneous upper crust
75 (e.g., Collanega et al., 2018; Heilman et al., 2019; Kolawole et al., 2018; Kolawole et al., 2021;



76 Morley, 2010; Morley, 1999). Pre-existing weak fabrics may appear as large shear zones (Daly
77 et al., 1989), suture zones along adjacent basement terranes (Corti, 2012; Corti et al., 2007) or
78 upper crustal fabrics. Recent strain accommodation in the Rukwa-North Malawi segment of the
79 western branch of the EARS (Fig. 1c) shows dominant dip-slip faulting parallel to the border
80 faults (Kolawole et al., 2018; Morley, 2010) driven by the reactivation of pre-existing basement
81 fabrics (Heilman et al., 2019). There, the concentration of seismicity in the SE and NW of the
82 Rukwa and Northern Malawi Rift, respectively suggest subsequent propagation and linkage of
83 the rift segments (Heilman et al., 2019 and references therein).

84

85 Rifts may form as initially isolated segments that propagate along strike, interact and evolve
86 into continuous zones of deformation with time as they link (Nelson et al., 1992). Rift segments
87 link through previously un-rifted interaction zones resulting in a characteristic geometry that
88 persists during later rift stages (Nelson et al., 1992). The interaction zone between the Ethiopian
89 and Kenyan rift of the eastern branch of the EARS comprises different sub-parallel deformed
90 regions (Fig. 1d). The western rift basin corresponds to the N-S trending Turkana Rift that
91 propagated northwestward from the Kenyan Rift via the Suguta Valley (Bonini et al., 2005;
92 Ebinger et al., 2000; Vetel and Le Gall, 2006). The eastern rift corresponds to the Kino Sogo
93 Fault Belt (KSFB) that propagated southward via the Chew Bahir as part of the Ethiopian Rift
94 (Ebinger et al., 2000; Moore Jr and Davidson, 1978; Saria et al., 2014). The two branches form
95 a double-armed system with the KSFB depicting a particular curved faulting style convex to the
96 west along long fault segments with only minor strain accommodation (Vétel et al., 2005).
97 However, the reason for the peculiar shape of the KSFB with its characteristic deformation style
98 remains unclear (Vétel et al., 2005).

99

100 Pre-existing fabrics as well as fault interaction across multiple scales disturb the regionally
101 inferred stress orientation (Morley, 2010; Olivia et al., 2022). In return, stress re-orientations
102 within and adjacent to rift segments influence the style of progressive deformation. Ultimately,
103 stress re-orientation may even favor pure dip-slip behavior even for extensional faults with an
104 oblique orientation to the regional extension (e.g., Corti et al., 2013; Morley, 2010, 2017;
105 Philippon et al., 2015). This interplay between pre-existing weak fabrics and local re-orientation
106 of the regional stress field affects how propagating rift segments interact. Under favorable
107 conditions, it may even cause deflection of propagating rift segments (Nelson et al., 1992).



108

109 Rift propagation and segment interaction has been investigated by analog modelling studies
110 that examined linkage of two segments across a transfer zone (e.g., Acocella et al., 1999;
111 Bellahsen and Daniel, 2005; Corti, 2012; Zwaan and Schreurs, 2017; Zwaan et al., 2016).
112 Bellahsen and Daniel (2005) studied the control of existing faults on new fault growth under
113 multiphase extension. They suggested that pre-existing faults may disturb the local stress field
114 and impede linkage of newly forming faults. While analog experiments are an effective tool to
115 simulate mechanical (brittle and ductile) deformation processes occurring in continental rifting
116 in 3D, accessing information about stresses is challenging. In contrast, numerical modelling
117 experiments provide direct access to element-wise stress tensors that can be interpreted in
118 terms of stress regimes and orientations under extension (Brune and Autin, 2013; Duclaux et
119 al., 2020). Despite the impact of stress distribution on faulting and rift segment interaction, only
120 recently numerical studies made use of it to gain further insights into rift evolution and
121 continental break-up (e.g., Brune, 2014; Brune and Autin, 2013; Glerum et al., 2020; Mondy et
122 al., 2018). However, these studies mostly focus on larger-scale deformation and evaluate
123 stresses over the entire time span of rifting up to continental break-up.

124

125 Here we use crustal-scale analog and numerical models to investigate rift propagation and
126 strain localization in early rifting stages when rift segments interact. Both types of models
127 document enigmatic rift segment deflection when two sub-parallel rift segments propagate
128 approximately in the same direction and compete for linkage with an opposingly propagating
129 segment. To understand the reason for rift segment deflection, we analyze the stress
130 distribution in early rifting stages and its interplay with strain localization that initiates above
131 pre-existing weak fabrics. Our experiments show that relatively simple rift segment interactions
132 can cause locally complex stress patterns that deviate from the regional stress field. Such stress
133 re-orientations occur in transient stages and can change over time and with progressive
134 deformation due to subsequent changes in material strengths.

135



136 2. Analog model

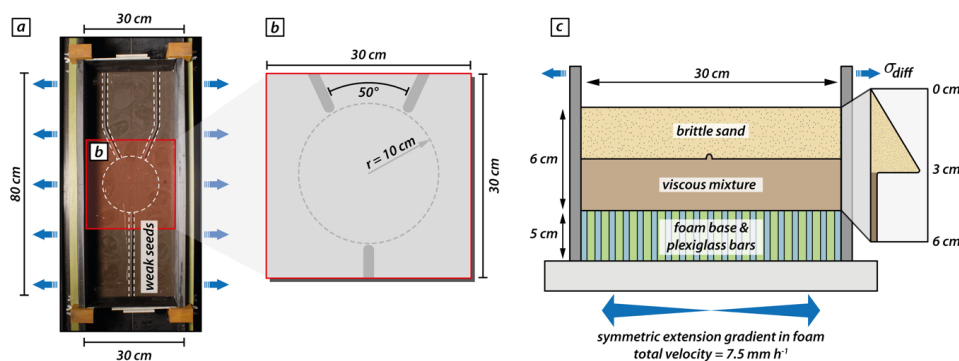
137 The presented analog modelling experiment shows unexpected features such as rift deflection.
138 It motivates our numerical study, and we use the analog model as a reference for examining
139 strain and stress distribution in numerical experiments.

140

141 2.1. Analog model setup

142 For the analog reference model, we use a simplified two-layer crustal scale setup with a brittle
143 and a viscous material to simulate upper crustal brittle faulting and lower crustal viscous
144 deformation, respectively. The base of the model consists of a set of alternating plexiglass and
145 foam bars which are compressed prior to the model preparation by two mobile sidewalls (Fig.
146 2a). During the experiment the computer-controlled sidewalls extend and provide a symmetric
147 extension gradient as the model base expands and the model vertically thins. For monitoring
148 the surface deformation evolution, we use a stereoscopic camera setup to take top view photos
149 and stereo image pairs every 60 s for quantitative deformation analysis by means of 3D stereo
150 Digital Image Correlation (Adam et al., 2005). The model was scanned every 20 min in a
151 medical XRCT scanner for gaining insights on internal model evolution.

152



153
154

155 **Figure 2:** Analog modelling setup. a) Top view of the experimental apparatus with two mobile side walls that extend
156 orthogonally. The entire model comprises an area of 80 x 30 cm and three viscous seeds are placed on top of the viscous layer
157 before sieving in the brittle sand layer. The central model part where propagating rift segments interact contains no seeds.
158 b) zoom in of the seed configuration into the analyzed model area (i.e., 30 x 30 cm). The two competing seed segments form
159 an intermediate angle of 50°. The model center contains an area with a radius of 10 cm where weak seeds are absent. c)
160 Sketch of the model cross section. The model setup consists of a brittle sand layer representing the upper brittle crust on top
161 of a viscous mixture of PDMS and corundum sand imitating the lower ductile crust.



162 **2.2. Model geometry, rheological layering, and material properties**

163 For simulating upper crustal deformation, we use dry quartz sand with a bulk density of 1560
164 kg m^{-3} and an internal friction coefficient of 0.72 (Schmid et al., 2020b). For the lower viscous
165 model part we use quasi-Newtonian PDMS/corundum sand mixture (weight ratio 1:1) with a bulk
166 density of 1600 kg m^{-3} and a viscosity of $1 \times 10^5 \text{ Pa s}$ (Zwaan et al., 2018). Hence, the brittle-
167 viscous setup has a density gradient that avoids density instabilities and spontaneous
168 upwelling of the viscous layer. The model features viscous rods placed on top of the viscous
169 model layer before sieving in the quartz sand. These rods act as mechanically weak seeds and
170 localize faulting in the upper brittle model domain. The used seed configuration includes three
171 individual seed segments. One model side includes a y-seed configuration with one seed
172 segment perpendicular to the extension direction (hereafter called frontal segment) whereas
173 on the opposing side of the model center two obliquely placed seeds (hereafter called rear
174 segments) form an intermediate angle of 50° (see also Fig. 1b&d). The three seed segments
175 hypothetically merge at the model center. However, we exclude weak seeds in an area with a
176 radius $r = 10 \text{ cm}$ around the model center to allow free interaction of the propagating rift
177 structures (Fig. 2b). The analog model comprises an initial area of 80 cm by 30 cm and has a
178 total thickness of 6 cm (each layer 3 cm) which represents a 30 km thick continental crust. In
179 accordance with the numerical setup, the effectively analyzed model area is restricted to $30 \times$
180 30 cm . The mobile sidewalls move with an extension velocity of 5 mm h^{-1} each (totaling in 10
181 mm h^{-1}), which results in a maximum extension of 40 mm at the final model stage after 4 h .

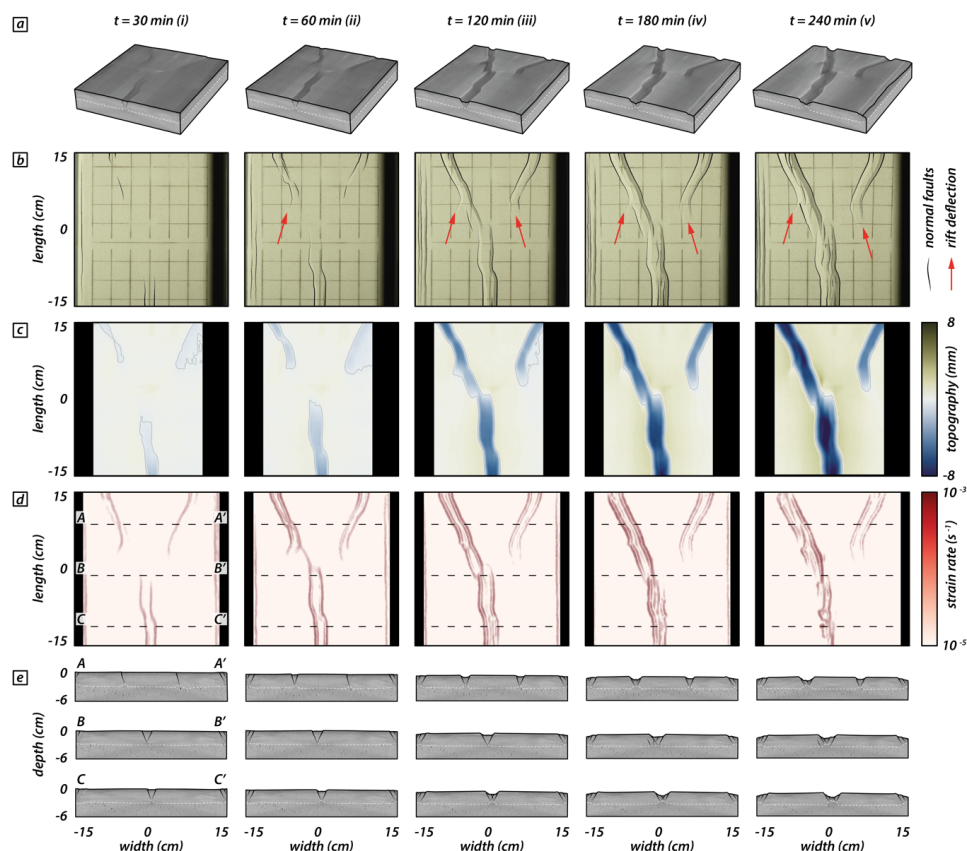
182

183 **2.3. Analog model results**

184 In the analog model three different rift segments initiate above the weak seeds and propagate
185 toward each other. Thereby, the two rear segments compete for linkage with the frontal
186 segment. After 30 min (i.e., 5 mm extension; Fig. 3(i)), brittle deformation localizes along two rift
187 boundary faults forming the frontal rift segment. Rifting in the rear segments localizes first along
188 right-dipping rift boundary faults and after 60 min (i.e., 10 mm extension; Fig. 3(ii)) both rear
189 segments develop a set of two conjugate rift boundary faults (Fig. 3a&b (ii)). Interestingly,
190 instead of advancing straight forward, the fault tips deflect and propagate away from each other
191 (Fig. 3b&d(ii)). This is partially due to the rift propagation over the area where no seeds are
192 present where rifting perpendicular to the extension direction is favored. However, after 120



193 min (i.e., 20 mm extension; Fig. 3 (iii)) rift tips deflect and turn away from one another. Rift tips
 194 deflect from an initially oblique orientation and rotate into an inverted oblique direction (with
 195 respect to the extension direction).
 196



197
 198
 199 **Figure 3:** Analog modelling results documenting deflection of the right rear segment and cessation of faulting activity. Distinct
 200 time steps (i.e., after 30 min and after every hour) show the model evolution. a) CT volumes of the investigated model domain
 201 at distinct time steps. White dashed lines indicate the brittle-viscous interface. b) Top views and line drawings indicating
 202 observable normal faults at the model surface. Red arrows indicate rift tips that deflect and turn away from one another. c)
 203 Topography from digital elevation models of the model surface. Colormap from Cramer et al. (2020). d) Strain rates obtained
 204 from 3D stereo DIC. Black dashed lines indicate positions of 3 transects through the CT volume. e) Rift transects A-A', B-B',
 205 and C-C'. White dashed lines indicate the brittle-viscous interface.

206
 207 The frontal and the rear left rift segment propagate further and, as they approach one another,
 208 form an en-echelon basin that convergently overlaps with the frontal rift segment (Morley et al.,



209 1990; Fig. 3b,d (iii)). After 180 min (i.e., 30 mm extension; Fig. 3(iv)), intra-rift faults develop in the
210 frontal and left rear rift segments. Note that strain rate is successively localized in the two fully
211 linked rift segments whereas the right rear segment experiences minor strain rate values (Fig.
212 3d (iv)). At the final model stage (i.e., after 240 min and 40 mm extension; Fig. 3 (v)), the right
213 rear segment propagated minimal with a rift tip turned away from the linked segments (Fig.
214 3b&d (v)). The fully linked frontal and left rear segments continuously accommodated
215 displacement resulting in deeper rift structures compared to the abandoned right rear segment
216 (Fig. 3c&e (v)).

217

218 **3. Numerical modelling**

219 We perform a series of numerical models to investigate rift linkage interaction and to analyze
220 occurring surface stresses. Similar to the analog experiment, the numerical model consists of a
221 two-layer crustal setup with laterally homogenous material layers where boundary-orthogonal
222 extension with constant velocity is applied.

223

224 **3.1. Numerical model setup**

225 We use the open source, finite-element code ASPECT to solve the extended Boussinesq
226 equations of momentum, mass, and energy in combination with advection equations for each
227 compositional field (Gassmüller et al., 2018; Glerum et al., 2020; Glerum et al., 2018; Heister et
228 al., 2017; Kronbichler et al., 2012; Rose et al., 2017). Since the numerical models are motivated
229 by the analog model, the two set ups are designed in a similar way. To this aim, we employ a
230 numerical setup where the rheologies of upper and lower crust are brittle and ductile,
231 respectively, and independent of temperature just like in the analog model. However, the
232 numerical models operate on the true scales of the continental crust over tens of kilometers
233 and millions of years, while the analog model is a scaled, cm-sized representation that evolves
234 on hour-scale. Additionally, the numerical set up applies maximum extension velocities at the
235 side walls and extension velocities at the base that linearly increase from the center towards
236 the model boundaries. In contrast, maximum extension velocities at the side walls in the analog
237 model are achieved via compression of a basal foam plexiglass setup (prior to the model run)
238 that extends homogeneously during the model run.

239



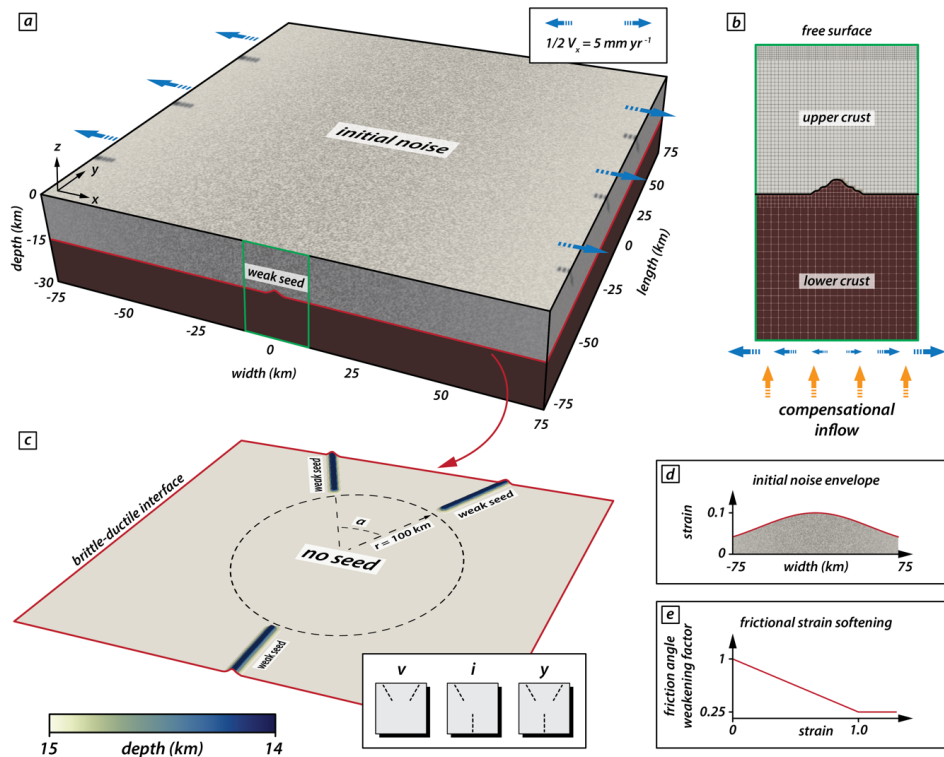
240 The presented numerical experiments cover a rectangular cuboid domain of 150 km width and
241 length in the horizontal x- and y-direction, respectively, and 30 km in depth along the vertical
242 z-axis (Fig. 4a). The entire model domain is divided into 1.53 million hexahedral, second-order
243 elements. For the upper 15 km of the model, we use a cell resolution of 750 m, with an additional
244 refinement at the uppermost km which yields near-surface elements with a resolution of 375 m
245 at the surface. The grid resolution for the lower 15 km of the model is 1500 m. At the left and
246 right model sides, we apply a symmetrically distributed outflow velocity of $\frac{1}{2} V_x = 5 \text{ mm yr}^{-1}$,
247 resulting in a total extension velocity of 10 mm yr^{-1} (Fig. 4a&b). After a total model time of 4 My,
248 the model has therefore experienced a total extension of 40 km. While V_x is prescribed at the
249 left and right model sides, V_y and V_z are allowed to move freely. We compensate material loss
250 through the side boundaries by compensational inflow at the model base and the horizontal V_x
251 component increases linearly from the model center towards the lateral model boundaries (Fig.
252 4b). The front and back lateral boundaries allow for free slip and the top of the model features
253 a free surface boundary condition (Rose et al., 2017).

254

255 The model includes two rheological layers represented by compositional fields, namely a 15
256 km thick visco-plastic upper crust with a density of 2700 kg m^{-3} and a 15 km thick iso-viscous
257 lower crust with a density of 2900 kg m^{-3} and a constant viscosity of $1 \cdot 10^{20} \text{ Pa s}$. For the upper
258 crust, the viscous viscosity is fixed to $2 \cdot 10^{28} \text{ Pa s}$, such that plastic deformation is always
259 enabled. We introduce initial and dynamic mechanical weaknesses in the upper crust in two
260 ways. (i) Mechanically weak seeds: At distinct positions near the brittle-ductile interface, the
261 upper model layer is locally 10% thinned and the lower model layer elevates like the viscous
262 weak seeds in the analog model setup. These mechanical seeds weaken the upper crustal
263 strength and localize brittle faulting. Our experiments include three different seed
264 configurations: v, i, and y (Fig. 4c; see also Fig. 1b-d), where seeds within a central model area
265 (i.e., $r = 100 \text{ km}$) are absent. For each configuration, the rear seeds form an intermediate angle
266 of 10° , 30° , or 50° . (ii) Friction softening: For each element, an initial plastic strain value of 0
267 (resulting in strong material) to 0.1 (weaker) is randomly assigned and reduces the maximum
268 friction angle of 26.56° by a maximum of 10%. This reflects the structural heterogeneity of
269 natural settings and allows for more randomized strain patterns in the central model domain
270 where the mechanical seeds are absent. The initial plastic strain noise is distributed over the



271 entire model width with an amplitude following a Gaussian curve parallel to the extension
 272 direction that is repeated along the model length (y-direction; Fig. 4d). During continuous
 273 extension, the effective friction angle linearly reduces to 25% of the maximum friction angle (i.e.
 274 to 6.64°) for plastic strain between 0 and 1 while it remains constant at 6.64° for plastic strains
 275 > 1 (Fig. 4e). This corresponds to a reduction of the effective friction coefficient from 0.5 to 0.12.
 276 The cohesion of the upper crust remains constant at $5 \cdot 10^6$ Pa for all conducted experiments.
 277



278
 279
 280 **Figure 4:** Numerical model setup for iso-viscous models. a) The model domain comprises a volume of $150 \times 150 \times 30$ km. Blue
 281 blue arrows indicate the applied boundary-orthogonal extension. The green rectangle indicates the position of the zoom-in in b).
 282 The red line indicates the initial depth of the brittle-ductile interface (as defined by the interface between the two rheological
 283 layers) indicated in c). b) Initial conditions and mesh refinement (arrows not to scale). c) Position and configuration of the
 284 mechanical weak seeds at the brittle-ductile interface. The setup comprises an area with radius $r = 100$ km where no weak
 285 seeds are present. Three different seed configurations refer to y-, i-, and v-models (see text for details). Colormap from
 286 Cramer *et al.* (2020). d) Initial amplitude of strain along the x-axis. The Gaussian distribution is constant along the y-axis;
 287 also see grey shade in a). Note that while the strain amplitude follows a Gaussian distribution, the location of the initial strain
 288 is random. e) Linear weakening with strain applied to the friction angle.



289 **3.2. Model limitations**

290 Just like the analog model (Sec. 2), our crustal scale two-layer numerical setup does not
291 comprise a lithospheric mantle layer and no asthenosphere. Further, the iso-viscous setup does
292 not account for a temperature-dependent viscosity. However, we focus on an early rifting phase
293 where the influence of the deforming mantle lithosphere can be neglected. The crustal-scale
294 setup strongly limits the computational effort for calculating deformation in 3D (Allken et al.,
295 2011, 2012; Katzman et al., 1995; Zwaan et al., 2016) and hence, our simplifications allow for a
296 higher model resolution; a necessity to depict early stages of rifting and the coalescence of
297 brittle deformation. Several alternative model runs have been performed including a
298 temperature- and pressure-dependent viscosity. Those tests reproduced first-order features
299 (i.e., strain rates, rift geometry and stress distribution) of the presented models in this study,
300 which further justified the choice of a simplified iso-viscous setup. Moreover, our model does
301 not include the influence of melting or magma intrusions nor sedimentation and erosion.

302

303 **3.3. Post-processing**

304 Numerical models pose the advantage that they grant direct access to stress tensors of each
305 individual cell. We exploit this opportunity by investigating surface stresses to deduct the stress
306 regime and the effect of different seed configurations on stress distribution. ASPECT provides
307 post processors that calculate the magnitude and orientation of the maximum horizontal
308 stresses and the Regime Stress Ratio (RSR) (Glerum et al., 2020). This stress regime
309 characterization is calculated according to the scheme of the World Stress Map (Zoback, 1992).
310 The RSR value maps possible stress regimes to an interval between 0 and 3. For isotropic and
311 homogenous materials, the standard rules of Andersonian faulting are applied (Anderson,
312 1905). For RSR values < 1 , faulting occurs in an extensional stress regime whereas for RSR
313 values > 2 compressive stress regimes generate thrust faults. Strike-slip faults occur for values
314 $1 \geq \text{RSR} \geq 2$. We extract data of maximum horizontal compressive stress together with the stress
315 regime and investigate them in areas where the strain rate exceeds a threshold of 10^{-16} s^{-1} and
316 deformation occurs.

317

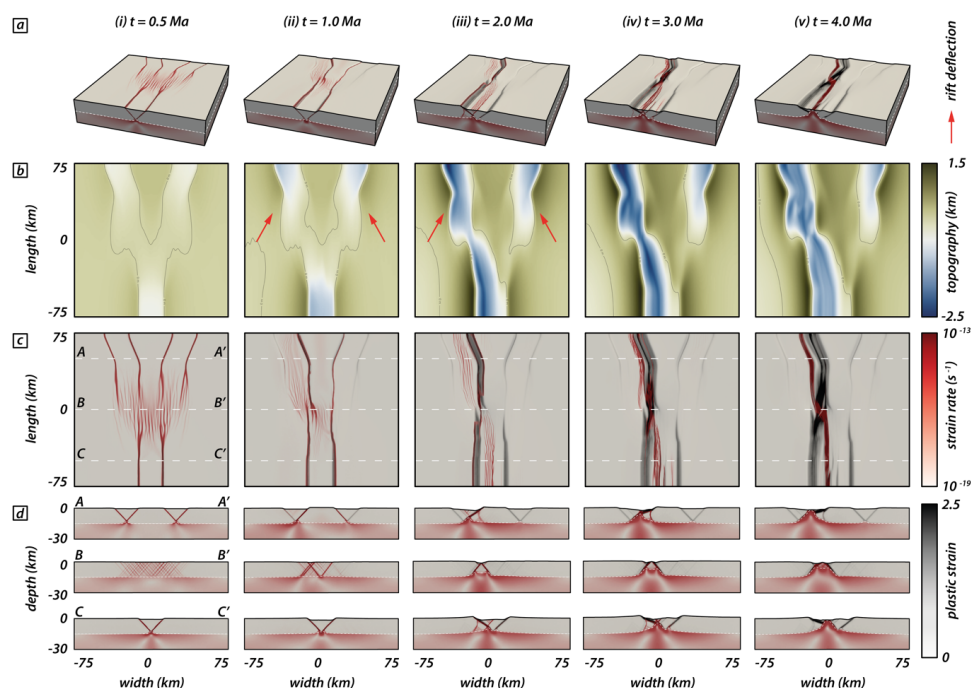


318 **3.4. General model evolution of the reference model**

319 In this section we describe the numerical modelling results focusing particularly on the general
320 evolution of our reference model with a y-seed configuration and an intermediate seed angle
321 of 50° (Figure 5). At the early stage (i.e., after 0.5 million years), three distinct rift segments
322 develop above the initial seed positions bounded by a pair of conjugate rift boundary faults
323 (Fig. 5a (i)). This early stage is characterized by a symmetric evolution of the two competing rear
324 segments, which results in a symmetric subsidence inside of the graben structures (Fig. 5b (i)).
325 For each rift segment, faulting activity is localized along the rift boundary faults. In the central
326 model domain, however, strain rates depict a more distributed deformation pattern with
327 multiple minor faults (Fig. 5c (i)). Note that the two rear segments propagate and show curved
328 fault segments that initially deflect and turn away from each other resulting in rift segments with
329 a curved geometry expressed in the topography (Fig. 5b (i)). Once they overlap with the
330 propagating frontal segment, faults symmetrically curve inwards and towards the frontal
331 segment. The change from localized strain rates above the seeds to distributed strain rate
332 patterns in the central model domain is best seen in transects (Fig. 5d (i)).

333

334 After the first million years, deformation has prominently localized along the left of the two rear
335 segments and along the frontal segment (Fig. 5a&c, (ii)). While deformation in the frontal
336 segment is localized along the rift boundary faults, inward migration occurred in the left rear
337 segment with developing intra-rift faults and only the left-dipping rift boundary fault active.
338 Similarly, the right rear segment shows faulting along the right-dipping rift boundary fault but
339 activity along intra-rift faults is lacking. In the central model domain, formerly distributed
340 deformation localized between the frontal and left rear rift segment (Fig. 5d (ii)). While strain
341 rates indicate a shift from a symmetric to an asymmetric deformation phase, topography is still
342 symmetric which implies that the shift is imminent and has not affected the topography after
343 the first million years (Fig. 5b (ii)).



344

345

346 **Figure 5:** Modelling results of the reference model documenting cessation of faulting activity along the right rear segment
 347 while the left rear, and frontal segments link. Distinct time steps show the model evolution. a) Model box showing logarithmic
 348 strain rates (red) and plastic strain (black) in the brittle and viscous model domain. White dashed lines indicate the brittle-
 349 viscous interface. b) Top views showing the model topography. Red arrows indicate rift tips that deflect and turn away from
 350 one another. Black lines refer to the zero elevation height. c) Top views of the model showing strain rates (red) and
 351 corresponding plastic strain (black) at distinct model run times. White dashed lines correspond to the three rift transects A-
 352 A', B-B', and C-C' in subfigure d). d) Rift-axis perpendicular transects A-A', B-B', and C-C' parallel to the extension direction.

353

354 After two million years, deformation is entirely localized along the frontal and left rear segment.
 355 Only the right-dipping rift boundary fault of the frontal segment is active and inward migration
 356 led to a set of pervasive intra-rift faults (Fig. 5a&c (iii)). The left rear segment depicts a similar
 357 deformation pattern as in the previous step, but strain mainly accumulates along the left-
 358 dipping rift boundary fault causing an asymmetric graben geometry (Fig. 5d (iii)). Note that, after
 359 two million years, fault activity along the right rear segment completely ceased with no further
 360 strain accumulation visible (Fig. 5a,c&d (iii)). The topography reflects this completed switch from
 361 a symmetric to an asymmetric deformation stage with enhanced subsidence along the frontal
 362 and left rear segments and their linkage throughout the central model domain (Fig. 5b (iii)).



363

364 With ongoing extension, deformation subsequently localizes along the axial rift zone that links
365 the frontal and left rear segments (Fig. 5a,c&d (iv,v)) and faulting activity along rift boundary
366 faults ceases. The linked structure reaches maximum depth inside of the rift after three million
367 years. After four million years, however, the basin experiences minor uplift due to increase
368 upward motion of the underlying viscous material (Fig. 5d (iv,v)). Note that the basin depth of
369 the right rear rift segment remains stable after two million years and does not experience further
370 subsidence nor uplift.

371

372 **3.5. Early localization patterns for v-, i-, and y-seeds**

373 To investigate the influence of different seed configurations, we compare v- (Fig. 6a-c), i- (Fig.
374 6d-f), and y-seed (Fig. 6g-i) configurations for different intermediate angles (i.e., 10°, 30°, and
375 50°) at an early stage after 0.5 million years. y- and i-seed configurations provide a setup where
376 rift structures opposingly propagate towards the model center where rift linkage eventually
377 occurs. In contrast, rift structures in the v-seed configuration propagate approximately in the
378 same direction, which has a consequence on the overall strain rate distribution.

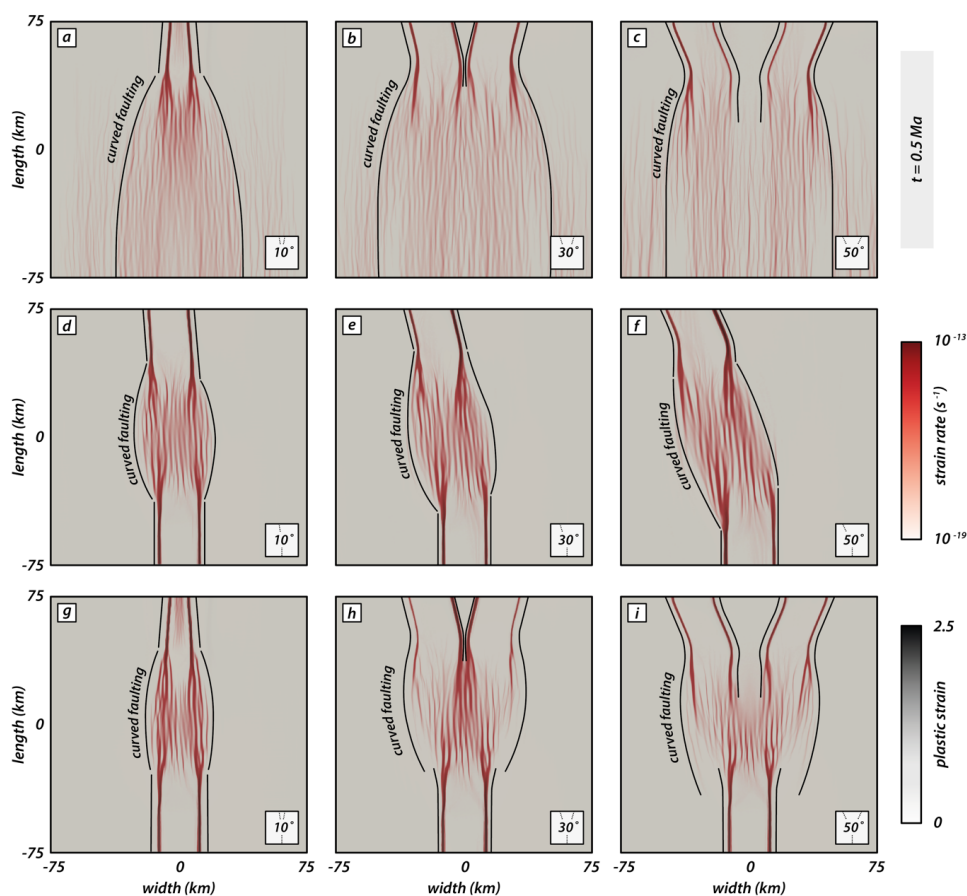
379

380 The early stage in v-seed experiments (Fig. 6a-c) is characterized by a zone of localized and
381 distributed deformation in the rear and frontal part of the experiments, respectively. The
382 transition from localized to distributed deformation occurs where the two competing rift
383 segments deflect and rotate away from one another. This is consistent with observations for
384 experiments with a y-seed configuration. However, there the two competing rear segments
385 rotate back and eventually bend towards the propagating frontal segment (Fig. 6g-i).

386

387 For experiment with a i-seed configuration (Fig. 6d-f) two opposingly propagating rift branches
388 form. Since the right rear segment is absent, both opposingly propagating rift segments link in
389 the model center where deformation is distributed onto intra-rift faults. The overall strain rate
390 field is localized, and no strain rate deflection occurs.

391



392
393

394 **Figure 6:** Types of rift segment linkages depending on the seed configuration at an early phase after 0.5 million years. Model
 395 top views show strain rates (logarithmic) and plastic strain in red and black colors, respectively. a-c) v-seed configuration for
 396 intermediate angles of 10°, 30°, and 50°. d-f) i-seed configuration for intermediate angles of 10°, 30°, and 50°. g-i) y-seed
 397 configuration for intermediate angles of 10°, 30°, and 50° (reference model). Black lines confine deformed areas. Curved
 398 faulting occurs where rift segments interact.

399

400 Models with a y-seed configuration (Fig. 6g-i) depict a strain rate pattern where deformation is
 401 localized along rift boundary faults at the model margins where seeds are present and a
 402 distributed en-echelon strain rate pattern in the model center. Note that for the model with an
 403 intermediate angle of 10° the two competing rear segments are close enough resulting in a
 404 zone where strain is localized along only one rift boundary fault per rift segment (i.e., outward-
 405 dipping faults with respect to the model box) that overlap and form a central graben with minor



406 intra-rift faults. For larger intermediate angles, two individual rift segments (bounded by two rift
407 boundary faults) form that propagate towards the model center. While the strain rate pattern
408 due to the competing rear segments is identical for experiments with a y- and v-seed
409 configuration, the additional frontal segment in experiments with a y-seed configuration causes
410 localization of strain rates in a single rift branch bounded by two rift boundary faults. This
411 contrasts with the v-seed configuration where strain rates in the frontal model domain occur
412 distributed over the entire model domain (Fig. 6a-c).

413

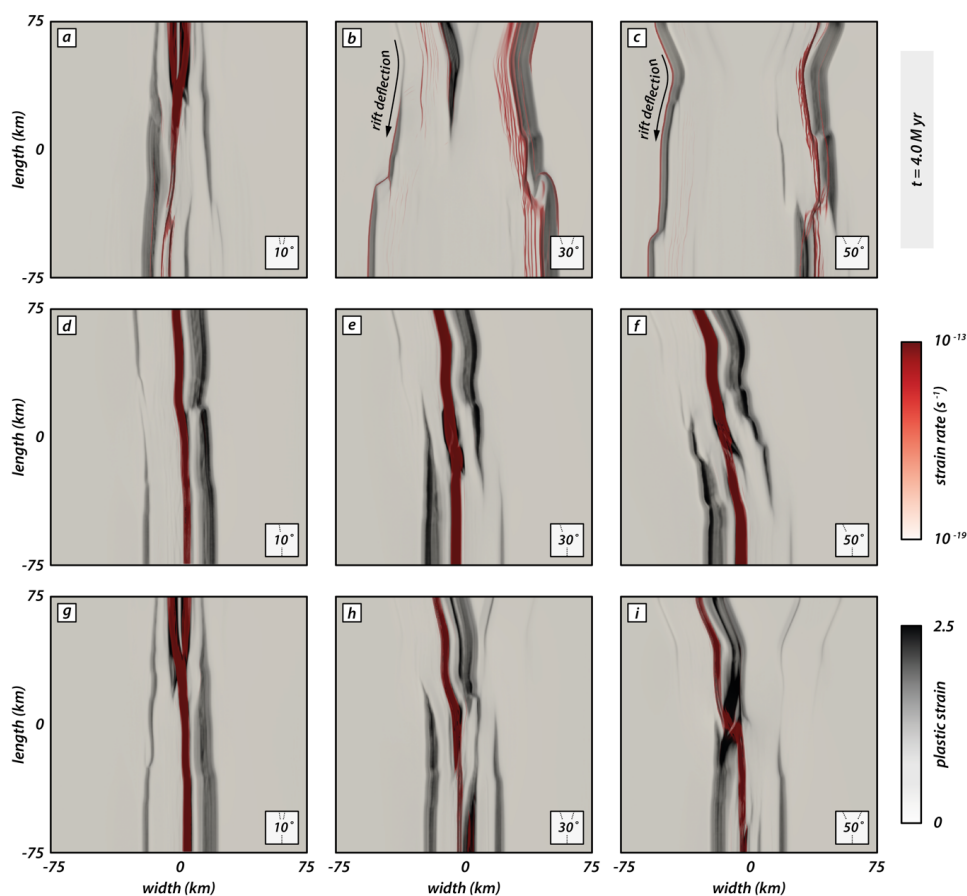
414 **3.6. Final rift geometry and localization patterns for v-, i-, and y-seeds**

415 The final model stage after four million years best illustrates differences in rift geometry
416 between the models with different seed geometry and an intermediate angle (Fig. 7). Rift
417 deflection is well visible in v-seed models (Fig. 7 a-c) and most prominent in experiments with
418 a larger intermediate angle (Fig. 7b&c). Above the seeds, two short individual rift segments form
419 bounded by a pair of conjugate rift boundary faults. However, as the rifts propagate towards
420 the model center, strain is mainly accommodated along the boundary faults that dip towards
421 the model center. Hence, the larger part of the model subsides uniformly and builds a broad
422 rift zone confined by two large boundary faults. When the two rift segments propagate, they
423 deflect and turn away from one another resulting in a gradually wider rift. For intermediate
424 angles of 30° and 50°, both competing rift segments show active faulting along intra-rift faults
425 in the rear model part, but a zone of continuous faulting activity has developed along the right
426 side of the rift.

427

428 Models with an i-seed configuration show a continuous and straight rift geometry for all
429 intermediate angles (fig. 7d-f). For an intermediate angle of 10°, the rift structure is nearly
430 orthogonal with respect to the extension direction. Note that most plastic strain is
431 accommodated along the left-dipping rift boundary fault (Fig. 7d). For larger intermediate
432 angles, the rift subsequently experiences more segmentation with small left stepping segments
433 towards the rear model part (Fig. 7e&f). Strain accommodation occurs mainly on the right-
434 dipping rift boundary fault for the frontal model part and switches to the left-dipping boundary
435 fault in the rear model part.

436



437

438 **Figure 7:** Influence of seed configuration on the final rift geometry after 4 million years. Strain rates (logarithmic) and plastic
439 strain are indicated by red, and black colors, respectively. a-c) v-seed configuration for intermediate angles of 10°, 30°, and
440 50°. d-f) i-seed configuration for intermediate angles of 10°, 30°, and 50°. g-i) y-seed configuration for intermediate angles
441 of 10°, 30°, and 50° (reference model).

442

443 The most prominent difference occurs in models with a y-seed configuration and various
444 intermediate angles. For an intermediate angle of 10°, the final rift geometry resembles that of
445 a continuous straight rift segment (Fig. 7g). Both competing rear seeds are close enough such
446 that they build one rift system rather than two distinct branches. For y-seed models with a larger
447 intermediate angle (Fig. 7h&i), two individual rear rift segments form and compete for linkage
448 with the frontal rift segment. Plastic strain well illustrates the asymmetric strain accommodation
449 focused along the left-dipping rift boundary fault of the left rear segment, whereas the right



450 rear segment only experienced minor strain accommodation (Fig. 7h&i). In both cases, high
451 strain rates are localized in the axial rift zone and witness activity along the linked frontal and
452 left rear segments.

453

454 Note that all experiments with an intermediate angle of 10° (Fig. 7a,d&g) form continuous
455 straight rift segments, regardless of the seed configuration. Additionally, the final rift geometry
456 for y- and v-seed configurations for an intermediate angle of 10° is similar with a gently wider
457 rift in the frontal model part (Fig. 7a&g). In contrast, for i-seed configurations the rift width is
458 similar along the entire length with a minor lateral offset (Fig. 7d). Strain rates are localized in
459 the axial rift zone throughout the entire model length forking into two close zones in the rear
460 end where the competing seeds are located.

461

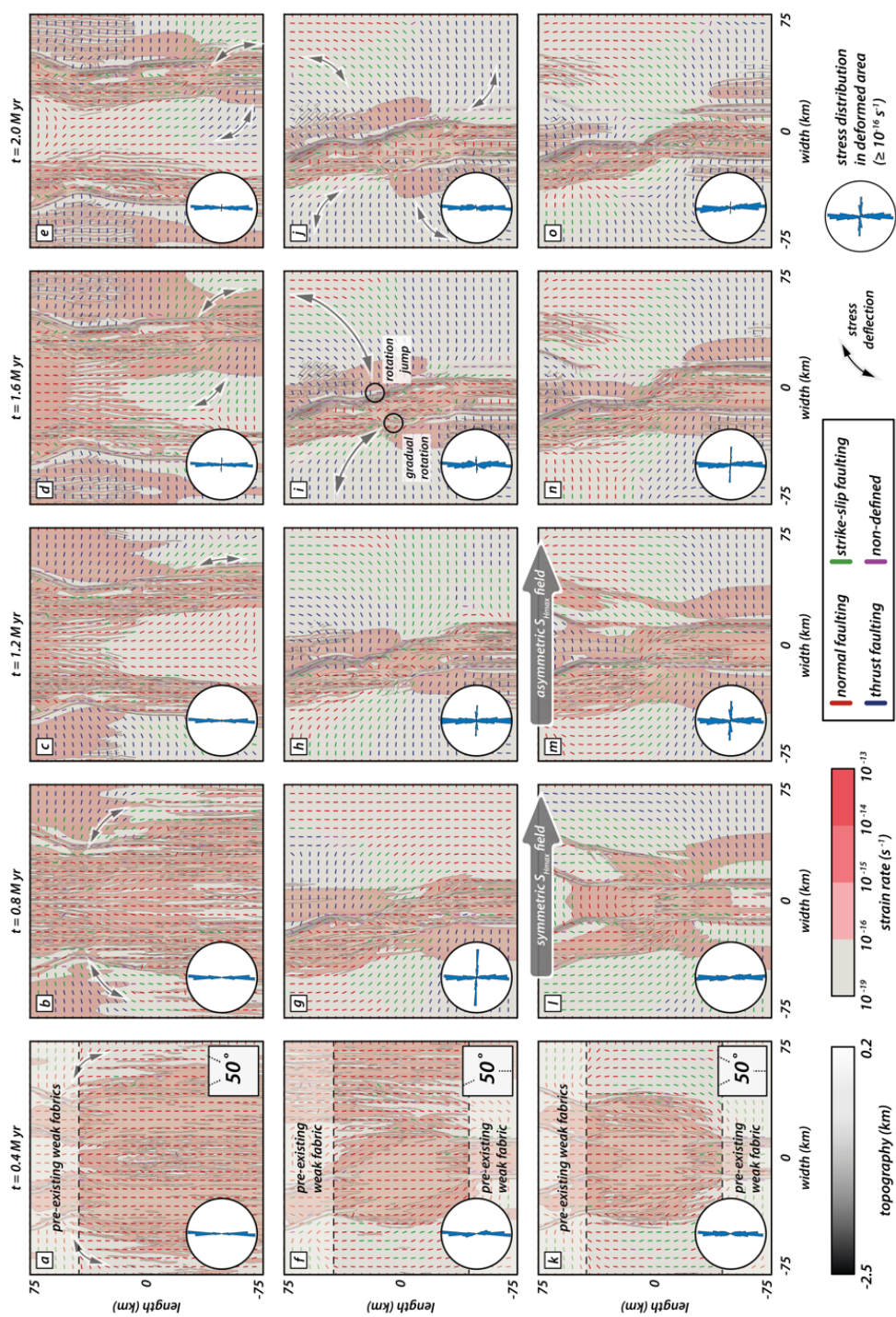
462 **3.7. S_{Hmax} evolution with progressive deformation**

463 In this section we present the distribution and orientation of the maximal horizontal
464 compressive stress component S_{Hmax} with progressive rift evolution and segment linkage. We
465 focus on models with v-, i-, and y-seed configurations and an intermediate angle of 50° (Fig. 8;
466 see also supplementary Figures S1-S3) distinguishing between model zones with pre-existing
467 weak fabrics (i.e., weak seeds) and a central zone where material strength is isotropic.

468

469 Our models depict two distinct phases within the first two million years: early strain
470 accommodation over a wider model domain followed by strain localization and linkage of
471 propagating rift segments (see also supplementary Figures S4-S6). Consequently, we focus on
472 S_{Hmax} in the first two million years of deformation and its effect on rift propagation. Figure 8
473 shows the orientation of S_{Hmax} and the stress regime based on the common color scheme of
474 the World Stress Map (Heidbach et al., 2018). Note that S_{Hmax} orientation and the stress regime
475 alone do not suffice to discriminate between locations where stresses exceed crustal strength
476 and faulting occurs. Strain rate values provide further necessary information, and we use a
477 threshold of 10^{-16} s^{-1} that splits the model into locations of active deformation (i.e., $\geq 10^{-16} \text{ s}^{-1}$) and
478 tectonically inactive domains (i.e., $< 10^{-16} \text{ s}^{-1}$).

479



480



481 **Figure 8:** Interplay of rift localization and surface stresses. Top views show the distribution of the maximum horizontal
482 compressive stress component S_{Hmax} (not scaled to the magnitude) in models with an intermediate angle of 50° at early
483 deformation stages (i.e., until 2 million years). a-e) v-seed configuration. f-j) i-seed configuration. k-o) y-seed configuration.
484 Black colors refer to topographic elevation and red colors mark zones where strain rates exceed a threshold of $10^{-16} s^{-1}$. Color
485 coding for the stress regime marks normal, strike-slip, and thrust faulting in red, green, and blue, respectively, using the
486 common color scheme of the World Stress Map (Heidbach et al., 2018). Elements where the stress regime is non-defined are
487 marked purple. Black arrows highlight stress deflection of S_{max} . Rose diagrams show the distribution of S_{Hmax} orientation in
488 zones where active faulting occurs (i.e., strain rate $\geq 10^{-16} s^{-1}$). Large grey arrows for the y-seed configuration mark the change
489 from a symmetric to an asymmetric S_{Hmax} distribution.

490

491 **3.7.1. Effect of S_{Hmax} re-orientation on rift propagation of competing rift segments**

492 **(v-seed models)**

493 Early stages in our numerical experiments are characterized by curved fault traces in the model
494 center where rift segments interact (see Fig. 6). Hereafter we refer to that phenomenon as
495 arcuate faulting. Arcuate faulting mainly occurs in experiments with larger intermediate angles
496 ($>10^\circ$) in early stages (Fig. 6), especially if two competing rift segments are present (v-, and y-
497 seed configurations). Moreover, we have shown that deflection of propagating rifts occurs
498 when deformation is symmetrically distributed along both competing rift branches. This is well
499 visible for the v-seed configuration (Fig. 8a-e). Assuming orthogonal extension and isotropic
500 material properties, S_{Hmax} is expected to align perpendicular to the extension direction
501 producing pure dip-slip normal faults (Anderson, 1905). However, the model shows an
502 immediate S_{Hmax} re-orientation at early deformation stages (i.e., after 0.4 million years; Fig. 8a)
503 from a N-S to a E-W orientation in the vicinity of the underlying weak seeds such that dip slip
504 faults are favored over oblique-slip faults with a strike-slip component. With progressive
505 extension (Fig. 8b-e), S_{Hmax} re-orientations successively propagate into the isotropic zone
506 without pre-existing fabrics, concomitant with the rift propagation. Consequently, the position
507 of the front where stress rotation occurs propagates over time resulting in the deflection of the
508 propagating rift arms away from each other.

509

510 There is a distinct difference between stress deflection along weak fabrics and E-W deflections
511 of S_{Hmax} in zones where strain rates are below the threshold. The v-seed configuration shows
512 localized strain accumulation along one rift boundary fault per segment (i.e., the outer one)
513 resulting in a rift zone with a broad graben system that subsides (Fig. 8e). S_{Hmax} re-orientation



514 inside of the graben is in parts identical to the E-W orientation of S_{Hmax} outside of the graben.
515 While local S_{Hmax} rotations may be explained by small differences in the maximum and
516 intermediate principal stress components, such E-W stress re-orientation in our model occurs
517 systematically and suggest that this feature reflects the influence of the strength anisotropy
518 (Morley, 2010). The initial S_{Hmax} deflection near weak fabrics locally favors dip-slip faulting but
519 also has regional influence on the overall stress regime.

520

521 **3.7.2. S_{Hmax} evolution in subparallel rift segments (i-seed models)**

522 During the early stage (i.e., after 0.4 million years, Fig. 8f), the distribution of S_{Hmax} resembles
523 the distribution from the v-seed configuration described in the previous section. Stress
524 deflection mainly occurs in zones where a weak fabric is present. S_{Hmax} values in the central
525 zone rotate by a small amount and reflect arcuate faulting (see Fig. 6). Since the two rift
526 segments propagate in opposing directions, linkage is efficient and localizes in a short time
527 (Fig. 8f-j). S_{Hmax} values deflect accordingly along propagating faults, which affects the entire
528 model domain. This deflection does not occur symmetrically on both sides of each rift segment.
529 Rather, it shows two distinct zones: 1) E-W orientations outside the rift deflect into a parallel
530 orientation near the rift boarder or 2) N-S orientations outside of the rift deflect into E-W
531 orientations near faults (Fig. 8j).

532

533 We find that S_{Hmax} orientations deflect gradually from E-W to N-S along abandoned rift boundary
534 faults where activity ceased (Fig. 8h-j; upper left and lower right model domain). In contrast,
535 S_{Hmax} re-orientations from N-S to nearly E-W towards active rift boundary faults are followed by
536 a rapid flip back to N-S along the faults (Fig. 8h-j; lower left and upper right model domain). The
537 two types of re-orientation seem to correspond with two types of deformed zones. Where
538 deformation is strongly localized along rift boundary faults, jumps in the S_{Hmax} orientation occur.
539 In contrast, zones where inward migration of fault activity activates intra-rift faults, S_{Hmax} re-
540 orientation occurs gradually.

541

542 **3.8. Rift arm competition and deflection (y-seed models)**

543 A prominent feature in our models with two competing rift segments is the deflection of rift
544 branches and arcuate strain rate patterns (Figs. 8a-e) in the model with a v-seed configuration.
545 Moreover, the i-seed configuration demonstrates a gradual S_{Hmax} re-orientation over a broader



546 pre-weakened zone due to formerly active boundary faults. One could therefore expect that
547 both features should occur in the model with y-seed configuration (Fig. 8k-o).

548

549 Indeed, early stages (i.e., after 0.4 million years; Fig. 8k) are characterized by a symmetric stress
550 field with re-oriented S_{Hmax} values near the two rear rift segments. However, in contrast to the
551 v-seed configuration, S_{Hmax} re-orientation also occurs near the frontal pre-existing weak fabric
552 along developing rift boundary faults. In the isotropic zone, S_{Hmax} values dominantly show a N-
553 S direction. The general N-S orientation reflects the regional stress field due to an E-W
554 extension as predicted by Anderson (1905) in isotropic areas where rift segments have not yet
555 propagated into. With ongoing extension, all three rift segments propagate into the isotropic
556 zone and cause a re-orientation of S_{Hmax} (Fig. 8l). Note that after 0.8 million years the stress re-
557 orientation occurs symmetrically. This contrasts with the i-seed configuration where S_{Hmax}
558 values deflect either into an E-W orientation along active rift boundary faults or gradually turn
559 into a fault parallel direction over a broader weakened zone (see subsection 3.7.). The early
560 symmetric stress distribution in the y-seed configuration model is unarguably due to the
561 symmetric seed configuration (see also Fig. 8a-e). It is only after 1.2 million years, when fault
562 activity along the right rear segment ceases that deformation localizes along the left rear and
563 frontal segments and linkage intensifies (Fig. 8m). Successively, localization and linkage occur
564 coevally with a switch from a symmetric to an asymmetric stress distribution and resembles
565 more the stress distribution in the i-seed configuration model (Fig. 8f-j). The model state after
566 1.2 million years (fig. 8m) also marks the switch from a symmetric to an asymmetric stress
567 distribution that was formerly dominated by the competing rear rift segments (i.e., v-seed
568 configuration) whereas after is dominated by the linkage of two obliquely oriented segments
569 (i.e., i-seed configuration).

570

571 This symmetry switch is also visible in rose diagrams of stress orientations within the active
572 faulting zone (i.e., strain rate $\geq 10^{-16} \text{ s}^{-1}$). A dominantly N-S oriented S_{Hmax} distribution changes to
573 a bimodal distribution with a second E-W orientation (Fig. 8l-n). Similarly, bimodal S_{Hmax}
574 distribution is also visible in the experiment with a i-seed configuration but occurs earlier. Since
575 the experiment with a i-seed configuration is never in the state of an early symmetric stress
576 distribution linkage is facilitated and occurs earlier (Fig.8g-i).

577



578 **4. Discussion**

579 Despite the relatively simple setup of our experiments, the interaction of individual weak seeds
580 generates a complex evolution of linkage patterns. In the following we discuss the effect of pre-
581 existing fabrics on S_{Hmax} re-orientations and how, in return, stress re-orientation influences rift
582 propagation and rift segment linkage.

583

584 **4.1. Effect of pre-existing fabrics on rift segment propagation, interaction, and S_{Hmax}**

585 Previous modelling studies demonstrated that pre-existing weaknesses may cause local re-
586 orientations of S_{Hmax} resulting in extensional faults with an oblique orientation to the regional
587 extension direction which exhibit pure dip-slip behavior (e.g., Corti et al., 2013; Morley, 2010,
588 2017; Philippon et al., 2015). This contrasts the expected (assuming Andersonian faulting theory)
589 occurrence of faults with an oblique slip component above pre-existing fabrics that are
590 obliquely oriented with respect to the extension direction (Tron and Brun, 1991; Withjack and
591 Jamison, 1986). Our S_{Hmax} analysis documents two types of stress re-orientation, either
592 gradually or by a jump along faults (Fig. 8i). A potential explanation for the two types of stress
593 deflection is that cessation of boundary fault activity (and subsequent faulting activity along
594 intra-rift faults) creates a broad zone of reduced crustal strength. Hence, S_{Hmax} orientations
595 successively re-orient along those formerly active faults and eventually rotate into a N-S
596 orientation along active intra-rift faults. In contrast, where faulting activity is strongly localized
597 along rift boundary faults, re-orientation occurs rapidly by a jump from E-W to a N-S orientation.
598 This suggests that formerly active faults act as a wider zone of pre-weakened material, where
599 stresses deflect sequentially rather than with a rapid jump. Similar observations have been
600 made in previous studies of numerical models (Gudmundsson et al., 2010; Kattenhorn et al.,
601 2000). These experiments suggest that earlier fractures lead to subzones (within a broader
602 damage zone), where stresses subsequently rotate away from the regional stress field.
603 Although our analog and numerical models do not feature elastic deformation, they indicate
604 that stress deflection is an ongoing process, even after elastic material failure. Such a stress
605 deflection further implies that stress orientations in rocks with pre-existing weaknesses can
606 substantially deviate from predicted orientations in isotropic media (Anderson (1905)).

607



608 It has been proposed that early faulting and propagation in the Rukwa and North Malawi Rifts
609 (Fig. 1c) were guided by pre-existing basement fabrics (Heilman et al., 2019). This region is
610 further shaped by a flip in the boundary fault polarity in the present-day geometry within the
611 interaction zone between Rukwa Rift and North Malawi Rift (Bosworth, 1985). Our i-seed models
612 show identical geometries for increasing intermediate angles (Fig. 7h&i), where plastic strain
613 near pre-existing weak fabrics is mostly accommodated along prominent rift boundary faults
614 that flip fault polarity from the frontal to the rear rift segment. Kolawole et al. (2018) further
615 propose two different types of strain accommodation at early rift phases. Prominent strain
616 accommodation localized onto a discrete and narrow zone along large rift boundary faults
617 (Style-1; sensu Kolawole et al., 2018) and faulting over a broader zone, where fault clusters may
618 reflect pre-conditioning of the material (Style-2; sensu Kolawole et al., 2018). With this
619 perspective, jumps and gradual rotation of S_{Hmax} orientations are comparable to Style-1 and
620 Style-2 strain localization, respectively, as proposed by Kolawole et al. (2018). Hence, the type
621 of weakness (narrow discrete zone or broad discrete zone) should also be reflected by the
622 stress re-orientation distribution (Morley, 2010).

623

624 **4.2. Local S_{Hmax} re-orientation and its influence on rift segment interaction and rift** 625 **deflection**

626 A particular observation in our experiments with a v-, and y-seed configuration is that two sub-
627 parallel rift segments, which propagate approximately in the same direction deflect away from
628 each other at early stages. This is somewhat surprising as one would expect the two rift
629 segments to cut towards each other by minimizing fault length. The occurrence of rift deflection
630 in both analog and numerical experiments validates that the results are robust and require
631 discussing the role of S_{Hmax} re-orientation and how it influences rift segment interaction.

632

633 We speculate that, while both rear rift segments in our y-seed models equivalently
634 accommodate strain in the early stages (i.e., when the overall stress distribution is symmetric;
635 Fig. 8), S_{Hmax} orientations are dominated by the influence of the two competing rear rift
636 segments that accommodate strain in equal parts. It is only after fault activity along one rear
637 segment ceases that deformation localizes along the active rear and frontal segments and
638 linkage intensifies. Strain localization and linkage occur coevally with a switch from a symmetric
639 to an asymmetric stress distribution resembling the stress distributions in v-, and i-seed



640 configuration models, respectively. The switch from a symmetric to an asymmetric stress
641 distribution in y-seed models also marks the switch from a system that was formerly dominated
642 by the competing rear rift segments (i.e., v-seed configuration) to a system that is dominated
643 by the linkage of two obliquely oriented segments (i.e., i-seed configuration).

644

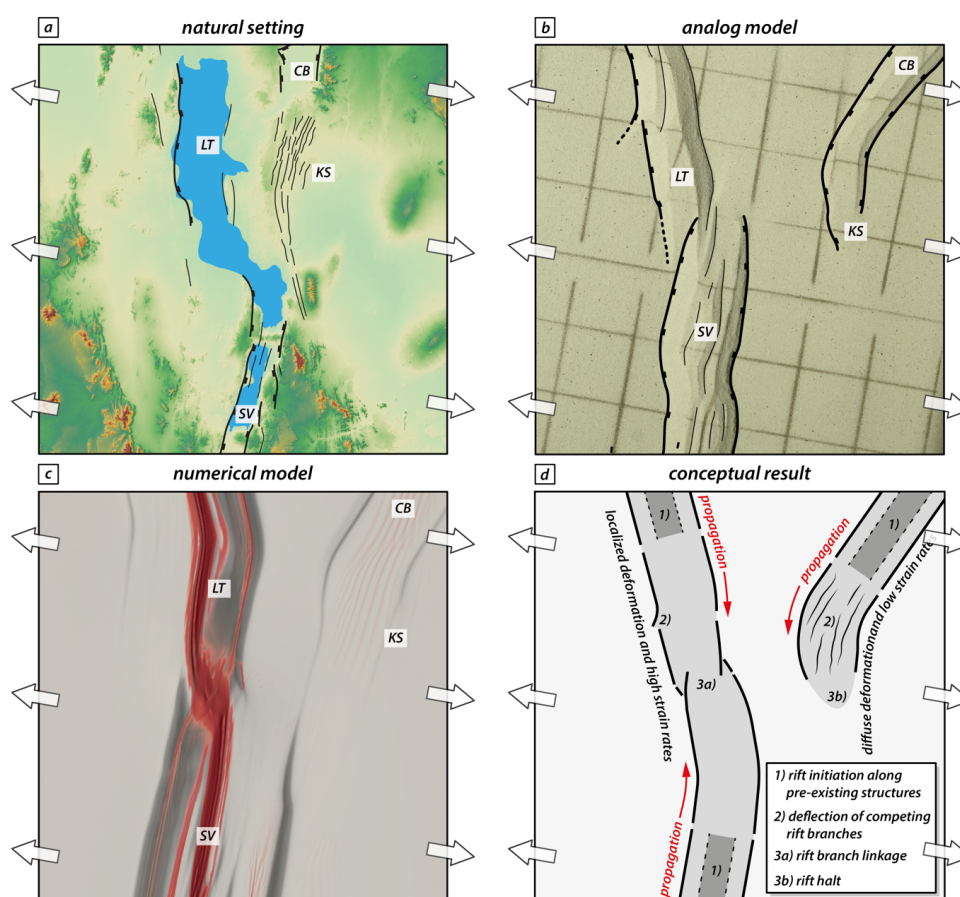
645 In models with a v-seed configuration, however, the symmetric phase prevails and causes
646 coeval S_{Hmax} re-orientations and rift deflection that cause divergence of the two propagating rift
647 segments. A similar process of extensional segment interaction via stress rotation is known
648 from mid-ocean ridge settings: Pollard and Aydin (1984) argue that paths of two opposingly
649 propagating oceanic ridges weakly diverge due to shear stresses that divert propagating ridges
650 as they approach each other. Once the two ridges overlap, the stress field changes causing
651 convergence and intersection. Similarly, Nelson et al. (1992) describe interference of
652 compressional zones of propagating cracks diverting their tips before they overlap and turn
653 back toward another. In this respect, our models with a v-seed configuration suggest that
654 stresses also cause divergence of two rift segments that propagate approximately in the same
655 direction. However, overlap never occurs (as they propagate approximately in the same
656 direction) and hence, the two segments remain in a stress field that further diverts their paths.

657

658 Only in models with a y-seed configuration, compressional zones and rift deflection can be
659 overcome once the opposingly propagating rift segment links with one of the competing rift
660 segments. Linkage occurs after about the first million years, concurrently with rift deflection and
661 abandonment of the right rear segment (Fig. 9b). Moreover, remaining activity in the right rear
662 segment depicts low strain rates along numerous arcuate intra-rift faults (Fig. 9c). This suggests
663 that linkage and rift abandonment are closely coupled and faulting along the linked segments
664 intensifies when the activity along the remaining rift segment ceases. With respect to the
665 Turkana Region this suggests that the KSFB may represent a southward propagating rift branch
666 that experienced a limited amount of extension-related deformation before propagation
667 aborted, similar to the neighboring Ririba Rift in the east (Corti et al., 2019). The definite linkage
668 of the Ethiopian and Kenyan Rift via the lake Turkana basin may represent a switch from a
669 symmetric to an asymmetric stress distribution after which local stress re-orientation favored
670 increased faulting activity along the linked system and caused the abandonment of the young
671 KSFB as seen in our models (Fig.9). Our modelling results show that stress deflection along rift



672 segment tips is a mechanical consequence of the interaction between weak zones and far-field
673 stresses offering a potential explanation for naturally occurring rift deflection such as seen in
674 the KSFB. However, we must emphasize that complexities in natural rift settings pose additional
675 difficulties that require further investigations of stress orientations.
676



677
678

679 **Figure 9:** Summary plot showing the geometric similarity of rift segment linkage, deflection of competing branches and
680 abandonment in natural setting, analog, and numerical models. a) Major rift segments in the Lake Turkana Rift system with
681 a double-armed rift system. CB: Chew Bahir basin; LT: Lake Turkana basin; KS: Kino Sogo Fault Belt; SV: Suguta Valley. b)
682 Observed key features at the final stage of the analog model. c) Final strain and strain rate pattern in the numerical reference
683 model. d) Conceptual interpretation of the Lake Turkana Rift based on our numerical results (for details see text).

684



685 Another example of rift deflection has been described in the Main Ethiopian Rift. Geophysical
686 and geologic studies evidence that pre-existing structures controlled the somewhat 11 Ma
687 southward propagation of the Northern Main Ethiopian Rift and its contemporaneous westward
688 deflection along the Yerer-Tullu Wellel Volcanotectonic Lineament (YTVL; Abebe et al., 1998;
689 Keranen and Klemperer, 2008; Muhabaw et al., 2022). Only after the rotation of the principal
690 stress direction at about 5-6 Ma (Bonini et al., 2005), extension along the YTVL ceased and
691 deformation localization along the Central Main Ethiopian Rift became more favorable. Our
692 models document similar rift deflections and moreover indicate that, even in the absence of
693 changing plate motions, rift segments deflect, and may cease while competing rift segments
694 prevail and strain further localizes.

695

696 For the Canyonlands National Park, it has been proposed that it is mainly the lateral offset
697 between pre-existing structures that explains the diversity of structures (Allken et al., 2013; Fig.
698 1b). With larger offsets, interaction between adjacent rift segments is limited and competing
699 grabens persist and endure ongoing propagation coevally. We find that stresses, in
700 combination with the geometry of pre-existing structures, play an important role and that they
701 have a mutual effect on one another. Hence, stress distribution must be considered as an
702 important factor especially in early rifting stages when segments link and predetermine strain
703 localization in following rifting phases.

704

705 **5. Conclusions**

706 We present a series of analog and numerical rifting experiments. Our results suggest that, even
707 in a relatively simple iso-viscous two-layer crustal setup, pre-existing weaknesses substantially
708 disturb the regional stress pattern, which impacts rift propagation and the overall rift evolution.
709 The complex stress re-orientation is distinct for different seed configurations (i.e., v-seed, i-
710 seed, and y-seed) and closely interacts with the final rift geometry. The most important findings
711 of our study can be summarized as follows:

712

- 713 • Our numerical experiments reproduce rift segment deflection seen in our analog
714 models. This highlights the robustness of our results and their applicability to



715 interpreting rift segment propagation, interaction, and linkage in natural settings of
716 continental rifting.

717 • Pre-existing fabrics may control localization of rift segments that successively
718 propagate into previously undeformed areas. Consequently, stress re-orientation
719 initially occurs along pre-conditioned zones and propagates, coevally with rift segment
720 propagation and strain accrual, into formerly undeformed areas.

721 • Interacting stresses between two competing rift segments may cause outward
722 deflection of the propagating rift tips resulting in a successively broader rift geometry
723 along-strike.

724 • Outward deflection of competing rift segments is less prominent if an opposingly
725 propagating rift segment is present. With progressive extensional deformation, strain
726 accrual along one of the competing rift segments prevails whilst faulting activity along
727 the other segment ceases. Coevally, the general stress orientation changes from a
728 symmetric to an asymmetric distribution indicating the onset of rift linkage.

729 • Our modelling results reproduce first-order structures of natural examples from the East
730 African Rift System and, on smaller scale, graben structures in the Canyonlands National
731 Park. The combined investigation of surface stresses and strain localization provides an
732 explanation for distinct rift deflection among competing rift segments and rift linkage
733 structures where ongoing deformation and stresses mutually affect each other.

734

735 While changes in rift orientation are often used to infer regional palaeo-movements, we
736 demonstrate that local stress field re-orientations can occur under constant plate motions. The
737 observed stress re-orientations change over time indicating that stresses measured in natural
738 examples may depict transient stages that change with progressive deformation due to
739 subsequent changes in material strengths.

740



741 **Data availability**

742 Rheological measurements of the used analog materials are available in the form of open
743 access data publications provided by the GFZ Data Service (brittle materials: Schmid et al.,
744 2020a; Schmid et al., 2020b; viscous materials: Zwaan et al., 2018).

745

746 **Competing interests**

747 The authors declare that they have no conflict of interest.

748

749 **Acknowledgements**

750 We thank Esther Heckenbach for helpful assistance with post processing and visualization. The
751 work was supported by the North-German Supercomputing Alliance (HLRN). We thank the
752 Swiss National Science Foundation for providing financial support.

753

754 **Funding**

755 This project is supported by the Swiss National Science Foundation [grant number
756 200021_178731].

757

758 **CRedit authorship contribution statement**

759 Timothy C. Schmid: Conceptualization, Methodology, Investigation, Formal Analysis, Writing –
760 original draft, Visualization, Data curation. Sascha Brune: Conceptualization, Methodology, HPC
761 funding acquisition, Supervision, Project administration, Writing – review & editing. Anne
762 Glerum: Methodology, Software, HPC funding acquisition, Writing – review & editing. Guido
763 Schreurs: Writing – review & editing, Supervision, Project administration, Funding acquisitions,
764 Resources.



765 References

766

767

768

769

770

771

772

773

774

775

776

777

778

779

780

781

782

783

784

785

786

787

788

789

790

791

792

793

794

795

796

797

798

799

800

801

802

803

804

805

806

807

808

809

810

811

812

813

814

815

816

817

818

819

820

821

822

823

824

825

826

827

828

829

830

831

832

833

834

835

836

837

838

839

- Abebe, T., Mazzarini, F., Innocenti, F., Manetti, P., 1998. The Yerer-Tullu Wellel volcanotectonic lineament: A transtensional structure in central Ethiopia and the associated magmatic activity. *Journal of African Earth Sciences* 26, 135-150. [https://doi.org/10.1016/S0899-5362\(97\)00141-3](https://doi.org/10.1016/S0899-5362(97)00141-3)
- Acocella, V., Faccenna, C., Funicello, R., Rossetti, F., 1999. Sand-box modelling of basement-controlled transfer zones in extensional domains. *Terra Nova-Oxford* 11, 149-156.
- Adam, J., Urai, J., Wieneke, B., Oncken, O., Pfeiffer, K., Kukowski, N., Lohrmann, J., Hoth, S., Van Der Zee, W., Schmatz, J., 2005. Shear localisation and strain distribution during tectonic faulting—New insights from granular-flow experiments and high-resolution optical image correlation techniques. *Journal of Structural Geology* 27, 283-301. <https://doi.org/10.1016/j.jsg.2004.08.008>
- Allken, V., Huisman, R.S., Fossen, H., Thieulot, C., 2013. 3D numerical modelling of graben interaction and linkage: a case study of the Canyonlands grabens, Utah. *Basin Research* 25, 436-449. <https://doi.org/10.1111/bre.12010>
- Allken, V., Huisman, R.S., Thieulot, C., 2011. Three-dimensional numerical modeling of upper crustal extensional systems. *Journal of Geophysical Research: Solid Earth* 116. <https://doi.org/10.1029/2011JB008319>
- Allken, V., Huisman, R.S., Thieulot, C., 2012. Factors controlling the mode of rift interaction in brittle-ductile coupled systems: A 3D numerical study. *Geochemistry, Geophysics, Geosystems* 13. <https://doi.org/10.1029/2012GC004077>
- Anderson, E.M., 1905. The dynamics of faulting. *Transactions of the Edinburgh Geological Society* 8, 387-402. <https://doi.org/10.1144/transed.8.3.387>
- Bellahsen, N., Daniel, J.M., 2005. Fault reactivation control on normal fault growth: an experimental study. *Journal of Structural Geology* 27, 769-780. <https://doi.org/10.1016/j.jsg.2004.12.003>
- Bonini, M., Corti, G., Innocenti, F., Manetti, P., Mazzarini, F., Abebe, T., Pecskey, Z., 2005. Evolution of the Main Ethiopian Rift in the frame of Afar and Kenya rifts propagation. *Tectonics* 24. <https://doi.org/10.1029/2004TC001680>
- Bosworth, W., 1985. Geometry of propagating continental rifts. *Nature* 316, 625-627. <https://doi.org/10.1038/316625a0>
- Brune, S., 2014. Evolution of stress and fault patterns in oblique rift systems: 3-D numerical lithospheric-scale experiments from rift to breakup. *Geochemistry, Geophysics, Geosystems* 15, 3392-3415. <https://doi.org/10.1002/2014GC005446>
- Brune, S., Autin, J., 2013. The rift to break-up evolution of the Gulf of Aden: Insights from 3D numerical lithospheric-scale modelling. *Tectonophysics* 607, 65-79. <https://doi.org/10.1016/j.tecto.2013.06.029>
- Brune, S., Corti, G., Ranalli, G., 2017. Controls of inherited lithospheric heterogeneity on rift linkage: Numerical and analog models of interaction between the Kenyan and Ethiopian rifts across the Turkana depression. *Tectonics* 36, 1767-1786. <https://doi.org/10.1002/2017TC004739>
- Childs, C., Watterson, J., Walsh, J., 1995. Fault overlap zones within developing normal fault systems. *Journal of the Geological Society* 152, 535-549. <https://doi.org/10.1144/gsjgs.152.3.0535>
- Collanega, L., Jackson, C.A.-L., Bell, R., Coleman, A.J., Lenhart, A., Breda, A., 2018. How do intra-basement fabrics influence normal fault growth? Insights from the Taranaki Basin, offshore New Zealand. <https://doi.org/10.31223/osf.io/8rn9u>
- Corti, G., 2012. Evolution and characteristics of continental rifting: Analog modeling-inspired view and comparison with examples from the East African Rift System. *Tectonophysics* 522-523, 1-33.



- 840 <https://doi.org/10.1016/j.tecto.2011.06.010>
841
842 Corti, G., Cioni, R., Franceschini, Z., Sani, F., Scaillet, S., Molin, P., Isola, I., Mazzarini, F., Brune, S., Keir, D., 2019.
843 Aborted propagation of the Ethiopian rift caused by linkage with the Kenyan rift.
844 *Nature communications* 10, 1-11.
845 <https://doi.org/10.1038/s41467-019-09335-2>
846
847 Corti, G., Philippon, M., Sani, F., Keir, D., Kidane, T., 2013. Re-orientation of the extension direction and pure
848 extensional faulting at oblique rift margins: Comparison between the Main Ethiopian Rift and laboratory
849 experiments.
850 *Terra Nova* 25, 396-404.
851 <https://doi.org/10.1111/ter.12049>
852
853 Corti, G., van Wijk, J., Cloetingh, S., Morley, C.K., 2007. Tectonic inheritance and continental rift architecture:
854 Numerical and analogue models of the East African Rift system.
855 *Tectonics* 26.
856 <https://doi.org/10.1029/2006TC002086>
857
858 Cramer, F., Shephard, G.E., Heron, P.J., 2020. The misuse of colour in science communication.
859 *Nature communications* 11, 1-10.
860 <https://doi.org/10.1038/s41467-020-19160-7>
861
862 Daly, M., Chorowicz, J., Fairhead, J., 1989. Rift basin evolution in Africa: the influence of reactivated steep
863 basement shear zones.
864 *Geological Society, London, Special Publications* 44, 309-334.
865 <https://doi.org/10.1144/GSL.SP.1989.044.01.17>
866
867 Duclaux, G., Huismans, R.S., May, D.A., 2020. Rotation, narrowing, and preferential reactivation of brittle structures
868 during oblique rifting.
869 *Earth and Planetary Science Letters* 531, 115952.
870 <https://doi.org/10.1016/j.epsl.2019.115952>
871
872 Ebinger, C., Yemane, T., Harding, D., Tesfaye, S., Kelley, S., Rex, D., 2000. Rift deflection, migration, and
873 propagation: Linkage of the Ethiopian and Eastern rifts, Africa.
874 *Geological Society of America Bulletin* 112, 163-176.
875 [https://doi.org/10.1130/0016-7606\(2000\)112<163:RDMAPL>2.0.CO;2](https://doi.org/10.1130/0016-7606(2000)112<163:RDMAPL>2.0.CO;2)
876
877 Gassmöller, R., Lokavarapu, H., Heien, E., Puckett, E.G., Bangerth, W., 2018. Flexible and scalable particle-in-cell
878 methods with adaptive mesh refinement for geodynamic computations.
879 *Geochemistry, Geophysics, Geosystems* 19, 3596-3604.
880 <https://doi.org/10.1029/2018GC007508>
881
882 Glerum, A., Brune, S., Stamps, D.S., Strecker, M.R., 2020. Victoria continental microplate dynamics controlled by
883 the lithospheric strength distribution of the East African Rift.
884 *Nature Communications* 11, 1-15.
885 <https://doi.org/10.1038/s41467-020-16176-x>
886
887 Glerum, A., Thieulot, C., Fraters, M., Blom, C., Spakman, W., 2018. Nonlinear viscoplasticity in ASPECT:
888 benchmarking and applications to subduction.
889 *Solid Earth* 9, 267-294.
890 <https://doi.org/10.5194/se-9-267-2018>
891
892 Gudmundsson, A., Simmenes, T.H., Larsen, B., Philipp, S.L., 2010. Effects of internal structure and local stresses on
893 fracture propagation, deflection, and arrest in fault zones.
894 *Journal of Structural Geology* 32, 1643-1655.
895 <https://doi.org/10.1016/j.jsg.2009.08.013>
896
897 Heidbach, O., Rajabi, M., Cui, X., Fuchs, K., Müller, B., Reinecker, J., Reiter, K., Tingay, M., Wenzel, F., Xie, F., 2018.
898 The World Stress Map database release 2016: Crustal stress pattern across scales.
899 *Tectonophysics* 744, 484-498.
900 <https://doi.org/10.1016/j.tecto.2018.07.007>
901
902 Heilman, E., Kolawole, F., Atekwana, E.A., Mayle, M., 2019. Controls of Basement Fabric on the Linkage of Rift
903 Segments.
904 *Tectonics* 38, 1337-1366.
905 <https://doi.org/10.1029/2018TC005362>
906
907 Heister, T., Dannberg, J., Gassmöller, R., Bangerth, W., 2017. High accuracy mantle convection simulation through
908 modern numerical methods—II: realistic models and problems.
909 *Geophysical Journal International* 210, 833-851.
910 <https://doi.org/10.1093/gji/ggx195>
911
912 Kattenhorn, S.A., Aydin, A., Pollard, D.D., 2000. Joints at high angles to normal fault strike: an explanation using 3-
913 D numerical models of fault-perturbed stress fields.
914 *Journal of structural Geology* 22, 1-23.
915 [https://doi.org/10.1016/S0191-8141\(99\)00130-3](https://doi.org/10.1016/S0191-8141(99)00130-3)
916



- 917 Katzman, R., ten Brink, U.S., Lin, J., 1995. Three-dimensional modeling of pull-apart basins: Implications for the
918 tectonics of the Dead Sea Basin.
919 *Journal of Geophysical Research: Solid Earth* 100, 6295-6312.
920 <https://doi.org/10.1029/94JB03101>
921
922 Keranen, K., Klemperer, S., 2008. Discontinuous and diachronous evolution of the Main Ethiopian Rift: Implications
923 for development of continental rifts.
924 *Earth and Planetary Science Letters* 265, 96-111.
925 <https://doi.org/10.1016/j.epsl.2007.09.038>
926
927 Koehn, D., Aanyu, K., Haines, S., Sachau, T., 2008. Rift nucleation, rift propagation and the creation of basement
928 micro-plates within active rifts.
929 *Tectonophysics* 458, 105-116.
930 <https://doi.org/10.1016/j.tecto.2007.10.003>
931
932 Kolawole, F., Atekwana, E.A., Laó-Dávila, D.A., Abdelsalam, M.G., Chindandali, P.R., Salima, J., Kalindekafe, L., 2018.
933 Active Deformation of Malawi Rift's North Basin Hinge Zone Modulated by Reactivation of Preexisting Precambrian
934 Shear Zone Fabric.
935 *Tectonics* 37, 683-704.
936 <https://doi.org/10.1002/2017TC004628>
937
938 Kolawole, F., Phillips, T.B., Atekwana, E.A., Jackson, C.A.-L., 2021. Structural inheritance controls strain distribution
939 during early continental rifting, rukwa rift.
940 *Frontiers in Earth Science*, 670.
941 <https://doi.org/10.3389/feart.2021.707869>
942
943 Kronbichler, M., Heister, T., Bangerth, W., 2012. High accuracy mantle convection simulation through modern
944 numerical methods.
945 *Geophysical Journal International* 191, 12-29.
946 <https://doi.org/10.1111/j.1365-246X.2012.05609.x>
947
948 Macdonald, K.C., Fox, P., 1983. Overlapping spreading centres: New accretion geometry on the East Pacific Rise.
949 *Nature* 302, 55-58.
950 <https://doi.org/10.1038/302055a0>
951 Mills, N., 1981. Dislocation array elements for the analysis of crack and yielded zone growth.
952 *Journal of Materials Science* 16, 1317-1331.
953 <https://doi.org/10.1007/BF01033848>
954
955 Mondy, L.S., Rey, P.F., Duclaux, G., Moresi, L., 2018. The role of asthenospheric flow during rift propagation and
956 breakup.
957 *Geology* 46, 103-106.
958 <https://doi.org/10.1130/G39674.1>
959
960 Moore Jr, J.M., Davidson, A., 1978. Rift structure in southern Ethiopia.
961 *Tectonophysics* 46, 159-173.
962 [https://doi.org/10.1016/0040-1951\(78\)90111-7](https://doi.org/10.1016/0040-1951(78)90111-7)
963
964 Morley, C., 2010. Stress re-orientation along zones of weak fabrics in rifts: An explanation for pure extension in
965 'oblique' rift segments?
966 *Earth and Planetary Science Letters* 297, 667-673.
967 <https://doi.org/10.1016/j.epsl.2010.07.022>
968
969 Morley, C., 2017. The impact of multiple extension events, stress rotation and inherited fabrics on normal fault
970 geometries and evolution in the Cenozoic rift basins of Thailand.
971 *Geological Society, London, Special Publications* 439, 413-445.
972 <https://doi.org/10.1144/SP439.3>
973
974 Morley, C., Nelson, R., Patton, T., Munn, S., 1990. Transfer zones in the East African rift system and their relevance
975 to hydrocarbon exploration in rifts.
976 *AAPG bulletin* 74, 1234-1253.
977 <https://doi.org/10.1306/OC9B2475-1710-11D7-8645000102C1865D>
978
979 Morley, C.K., 1999. Patterns of displacement along large normal faults: implications for basin evolution and fault
980 propagation, based on examples from East Africa.
981 *AAPG bulletin* 83, 613-634.
982 <https://doi.org/10.1306/00AA9C0A-1730-11D7-8645000102C1865D>
983
984 Muhabaw, Y., Muluneh, A.A., Nugsse, K., Gebru, E.F., Kidane, T., 2022. Paleomagnetism of Gedemsa magmatic
985 segment, Main Ethiopian Rift: Implication for clockwise rotation of the segment in the Early Pleistocene.
986 *Tectonophysics* 838, 229475.
987 <https://doi.org/10.1016/j.tecto.2022.229475>
988
989 Nelson, R., Patton, T., Morley, C., 1992. Rift-segment interaction and its relation to hydrocarbon exploration in
990 continental rift systems.
991 *AAPG bulletin* 76, 1153-1169.
992 <https://doi.org/10.1306/BDF898E-1718-11D7-8645000102C1865D>
993



- 994 Olivia, S. J., Ebinger, C. J., Rivalta, E., Williams, C. A., Wauthier, C., Currie, C. A., 2022. State of stress and stress
995 rotations: Quantifying the role of surface topography and subsurface density contrasts in magmatic rift zones
996 (Eastern Rift, Africa).
997 *Earth and Planetary Science Letters*, 584, 117478.
998 <https://doi.org/10.1016/j.epsl.2022.117478>
999
- 1000 Philippon, M., Willingshofer, E., Sokoutis, D., Corti, G., Sani, F., Bonini, M., Cloetingh, S., 2015. Slip re-orientation in
1001 oblique rifts.
1002 *Geology* 43, 147-150.
1003 <https://doi.org/10.1130/G36208.1>
1004
- 1005 Pollard, D. D., Aydin, A., 1984. Propagation and linkage of oceanic ridge segments.
1006 *Journal of Geophysical Research: Solid Earth* 89, 10017-10028.
1007 <https://doi.org/10.1029/JB089iB12p10017>
1008
- 1009 Rose, I., Buffett, B., Heister, T., 2017. Stability and accuracy of free surface time integration in viscous flows.
1010 *Physics of the Earth and Planetary Interiors* 262, 90-100.
1011 <https://doi.org/10.1016/j.pepi.2016.11.007>
1012
- 1013 Rosendahl, B.R., 1987. Architecture of continental rifts with special reference to East Africa.
1014 *Annual Review of Earth and Planetary Sciences* 15, 445.
1015 <https://doi.org/10.1146/annurev.ea.15.050187.002305>
1016
- 1017 Saria, E., Calais, E., Stamps, D., Delvaux, D., Hartnady, C., 2014. Present-day kinematics of the East African Rift.
1018 *Journal of Geophysical Research: Solid Earth* 119, 3584-3600.
1019 <https://doi.org/10.1002/2013JB010901>
1020
- 1021 Schmid, T., Schreurs, G., Warsitzka, M., Rosenau, M., 2020a. Effect of sieving height on density and friction of
1022 brittle analogue material: Ring-shear test data of corundum sand used for analogue experiments in the Tectonic
1023 Modelling Lab of the University of Bern (CH).
1024 *GFZ Data Services*.
1025 <https://doi.org/10.5880/fidgeo.2020.005>
1026
- 1027 Schmid, T., Schreurs, G., Warsitzka, M., Rosenau, M., 2020b. Effect of sieving height on density and friction of
1028 brittle analogue material: ring-shear test data of quartz sand used for analogue experiments in the Tectonic
1029 Modelling Lab of the University of Bern (CH).
1030 *GFZ Data Services*.
1031 <https://doi.org/10.5880/fidgeo.2020.006>
1032
- 1033 Schultz-Ela, D., Walsh, P., 2002. Modeling of grabens extending above evaporites in Canyonlands National Park,
1034 Utah.
1035 *Journal of Structural Geology* 24, 247-275.
1036 [https://doi.org/10.1016/S0191-8141\(01\)00066-9](https://doi.org/10.1016/S0191-8141(01)00066-9)
1037
- 1038 Tron, V., Brun, J.-P., 1991. Experiments on oblique rifting in brittle-ductile systems.
1039 *Tectonophysics* 188, 71-84.
1040 [https://doi.org/10.1016/0040-1951\(91\)90315-J](https://doi.org/10.1016/0040-1951(91)90315-J)
1041
- 1042 Trudgill, B.D., 2002. Structural controls on drainage development in the Canyonlands grabens of southeast Utah.
1043 *AAPG bulletin* 86, 1095-1112.
1044 <https://doi.org/10.1306/61EEDC2E-173E-11D7-8645000102C1865D>
1045
- 1046 Vetel, W., Le Gall, B., 2006. Dynamics of prolonged continental extension in magmatic rifts: the Turkana Rift case
1047 study (North Kenya).
1048 *Geological Society, London, Special Publications* 259, 209-233.
1049 <https://doi.org/10.1144/GSL.SP.2006.259.01.17>
- 1050 Vétel, W., Le Gall, B., Walsh, J.J., 2005. Geometry and growth of an inner rift fault pattern: the Kino Sogo Fault Belt,
1051 Turkana Rift (North Kenya).
1052 *Journal of Structural Geology* 27, 2204-2222.
1053 <https://doi.org/10.1016/j.jsg.2005.07.003>
1054
- 1055 Willemse, E.J., 1997. Segmented normal faults: Correspondence between three-dimensional mechanical models
1056 and field data.
1057 *Journal of Geophysical Research: Solid Earth* 102, 675-692.
1058 <https://doi.org/10.1029/96JB01651>
1059
- 1060 Willemse, E.J., Pollard, D.D., Aydin, A., 1996. Three-dimensional analyses of slip distributions on normal fault arrays
1061 with consequences for fault scaling.
1062 *Journal of Structural Geology* 18, 295-309.
1063 [https://doi.org/10.1016/S0191-8141\(96\)80051-4](https://doi.org/10.1016/S0191-8141(96)80051-4)
1064
- 1065 Withjack, M.O., Jamison, W.R., 1986. Deformation produced by oblique rifting.
1066 *Tectonophysics* 126, 99-124.
1067 [https://doi.org/10.1016/0040-1951\(86\)90222-2](https://doi.org/10.1016/0040-1951(86)90222-2)
1068
- 1069 Zoback, M.L., 1992. First-and second-order patterns of stress in the lithosphere: The World Stress Map Project.
1070 *Journal of Geophysical Research: Solid Earth* 97, 11703-11728.



1071 <https://doi.org/10.1029/92JB00132>
1072 Zwaan, F., Schreurs, G., 2017. How oblique extension and structural inheritance influence rift segment interaction:
1073 Insights from 4D analog models.
1074 *Interpretation* 5, SD119-SD138.
1075 <https://doi.org/10.1190/INT-2016-0063.1>
1076
1077 Zwaan, F., Schreurs, G., Naliboff, J., Buiter, S.J.H., 2016. Insights into the effects of oblique extension on continental
1078 rift interaction from 3D analogue and numerical models.
1079 *Tectonophysics* 693, 239-260.
1080 <https://doi.org/10.1016/j.tecto.2016.02.036>
1081
1082 Zwaan, F., Schreurs, G., Ritter, M., Santimano, T., Rosenau, M., 2018. Rheology of PDMS-corundum sand mixtures
1083 from the Tectonic Modelling Lab of the University of Bern (CH).
1084 *GFZ Data Services*.
1085 <http://doi.org/10.5880/figgeo.2018.023>